

The Solar Wind Ion Analyzer for MAVEN

J.S. Halekas · E.R. Taylor · G. Dalton · G. Johnson ·
D.W. Curtis · J.P. McFadden · D.L. Mitchell · R.P. Lin ·
B.M. Jakosky

Received: 29 August 2013 / Accepted: 7 November 2013
© Springer Science+Business Media Dordrecht 2013

Abstract The Solar Wind Ion Analyzer (SWIA) on the MAVEN mission will measure the solar wind ion flows around Mars, both in the upstream solar wind and in the magnetosheath and tail regions inside the bow shock. The solar wind flux provides one of the key energy inputs that can drive atmospheric escape from the Martian system, as well as in part controlling the structure of the magnetosphere through which non-thermal ion escape must take place. SWIA measurements contribute to the top level MAVEN goals of characterizing the upper atmosphere and the processes that operate there, and parameterizing the escape of atmospheric gases to extrapolate the total loss to space throughout Mars' history. To accomplish these goals, SWIA utilizes a toroidal energy analyzer with electrostatic deflectors to provide a broad $360^\circ \times 90^\circ$ field of view on a 3-axis spacecraft, with a mechanical attenuator to enable a very high dynamic range. SWIA provides high cadence measurements of ion velocity distributions with high energy resolution (14.5 %) and angular resolution ($3.75^\circ \times 4.5^\circ$ in the sunward direction, $22.5^\circ \times 22.5^\circ$ elsewhere), and a broad energy range of 5 eV to 25 keV. Onboard computation of bulk moments and energy spectra enable measurements of the basic properties of the solar wind at 0.25 Hz.

Keywords Mars · Solar wind · MAVEN mission · Electrostatic analyzer

1 Introduction to the Solar Wind Ion Analyzer (SWIA)

1.1 Scientific Objectives

The scientific objectives of the Mars Atmosphere and Volatile Evolution (MAVEN) mission (Jakosky et al. 2014) include determining the current state of the upper atmosphere and the

J.S. Halekas (✉) · E.R. Taylor · G. Dalton · G. Johnson · D.W. Curtis · J.P. McFadden · D.L. Mitchell ·
R.P. Lin
Space Sciences Laboratory, University of California, 7 Gauss Way, Berkeley, CA 94720, USA
e-mail: jazzman@ssl.berkeley.edu

B.M. Jakosky
Laboratory for Atmospheric and Space Physics, University of Colorado, 1234 Innovation Dr., Boulder,
CO 80303, USA

processes that control it, measuring the escape rate of atmospheric gases to space during the present epoch and determining how the escape rate depends on the controlling processes, and extrapolating the total atmospheric loss to space over Mars' history. The solar wind provides one of the main drivers of the induced magnetosphere of Mars, by directly ionizing atmospheric constituents through the process of charge exchange (Zhang et al. 1993; Kallio et al. 1997), and by defining the convection flow that picks up newly ionized atmospheric constituents and in part controls the formation of the Martian bow shock and magnetosphere (Dubinin et al. 2006) through which atmospheric ions must travel to escape (Fang et al. 2010). The main role of the Solar Wind Ion Analyzer (SWIA) on MAVEN is to measure the flux of solar wind ions (primarily protons) to the Martian system, enabling parameterization of atmospheric escape channels as a function of solar wind input for extrapolation back in time. SWIA provides complementary measurements to those from the mass-resolving STATIC instrument (McFadden et al. 2014), which will focus on planetary ions derived from the Martian upper atmosphere.

Previous missions, including Mars Express, have characterized much of the overall morphology of the environment that MAVEN will encounter in its orbit around Mars (Dubinin et al. 2006; Fedorov et al. 2006; Lundin et al. 2008). For most of its mission, MAVEN will spend a portion of its orbit in the upstream solar wind, a portion in the magnetosheath, and a portion deep in the magnetosphere and ionosphere. As a result, SWIA will have to measure distributions varying from a very cold beam in the upstream solar wind (with typical velocities of $\sim 250\text{--}600$ km/s, densities of $\sim 1\text{--}20$ particles per cubic centimeter, and temperatures on the order of $50,000\text{--}200,000$ K) to the thermalized and slower (but still solar-wind derived) plasma that dominates the sheath. The solar wind typically contains about $\sim 4\%$ He^{++} , roughly co-moving with the protons. SWIA does not have mass resolution capability, but can distinguish alpha particles from solar wind protons based on their energy/charge (twice that of the protons), as long as the thermal velocity remains small compared to the bulk velocity. As MAVEN nears the planet, its ion instruments will have to measure an increasingly dominant population of heavier planetary ions derived from the Martian atmosphere. SWIA cannot distinguish these heavy ions from protons without recourse to data from other instruments, except in cases where they have a clearly different energy per charge (e.g., pickup ions). In this environment, the mass-resolving STATIC instrument (McFadden et al. 2014) will provide the primary ion measurement; however, by utilizing STATIC data to constrain the composition, SWIA can still contribute useful data in the low-altitude portion of the orbit, especially for the (relatively common) case where the two instruments have complementary fields of view.

SWIA's measurements contribute to the goal of understanding the current state of the upper atmosphere, as part of a full suite of plasma instrumentation including STATIC (McFadden et al. 2014), SWEA (Mitchell et al. 2014), LPW (Andersson et al. 2014), SEP (Larson et al. 2014), and MAG (Connerney et al. 2014). SWIA will make measurements of the ion dynamic pressure that, together with the interplanetary magnetic field, controls the overall structure of the Martian magnetosphere (Nagy et al. 2004; Brain et al. 2005), and can drive enhanced escape (Edberg et al. 2010). SWIA will also make measurements relevant to individual non-thermal ion escape channels, including but not limited to ion pickup (Lammer and Bauer 1991; Lundin et al. 1990) and subsequent sputtering (Luhmann and Kozyra 1991; Leblanc and Johnson 2001), magnetic reconnection (Eastwood et al. 2008; Brain et al. 2010; Halekas et al. 2009; Dubinin et al. 2012), auroral processes (Brain et al. 2006; Lundin et al. 2006; Dubinin et al. 2009) (particularly in regions with significant crustal magnetic fields (Acuña et al. 1999)), wave-particle interactions (Espley et al. 2004; Ergun et al. 2006), shear-driven boundary layer processes (Penz et al. 2004; Gunell et al. 2008;

Halekas et al. 2011), and plasma sheet acceleration (Dubinin et al. 1993; Fedorov et al. 2006). No previous mission has had the complete suite of magnetic field and charged particle measurements and the seasonal and local time coverage that MAVEN can bring to bear to fully characterize these escape channels.

1.2 Driving Requirements

The scientific goals of the MAVEN mission and the spacecraft accommodation each drive specific elements of the SWIA instrument design. In order to resolve the solar wind flow from the undisturbed interplanetary medium inward to the stagnation point, SWIA must measure proton velocities ranging from 50–1000 km/s, equivalent to an energy range of 13–5000 eV. In order to measure the slowest flows in the magnetosheath as well as the highest fluxes expected during cold dense solar wind flows, SWIA must have sensitivity to differential energy fluxes of 10^5 – 10^{11} eV/[cm² s sr eV]. SWIA achieves this large dynamic range by utilizing high-current microchannel plate detectors and preamplifiers capable of counting at MHz rates, together with a mechanical attenuator to provide a variable sensitivity. To measure the details of the ion distribution and its spatial variability, SWIA must provide good energy, angle, and time resolution. Lastly, to accomplish these goals on a non-spinning platform, SWIA requires a broad angular field of view, driving the selection of a design with electrostatic deflectors.

1.3 Heritage

The SWIA instrument utilizes heritage elements and design practices from many generations of electrostatic analyzers built at the U.C. Berkeley Space Sciences Laboratory, including PESA-H and PESA-L from Wind (Lin et al. 1995) and the ESA instruments for the FAST (Carlson et al. 2001) and THEMIS (McFadden et al. 2008) missions. Of these predecessor instruments, SWIA shares the most with THEMIS ESA, including many elements of the anode board design, the preamplifier circuit, and the high voltage supply design. SWIA and STATIC both utilize a toroidal analyzer with the same geometry (though different scale) as the Cluster CIS instrument (Rème et al. 1997). SWIA's ion deflectors represent a new development (FAST utilized deflectors to sweep a much smaller range), as does its mechanical attenuator.

2 SWIA Instrument Description

2.1 Overview

The SWIA instrument, as shown in the simplified block diagram of Fig. 1, consists of a cylindrically symmetric electrostatic analyzer with deflection optics, an annular microchannel plate (MCP) detector mounted to an anode board, and four additional electronics boards in an attached electronics box that produce and control low and high voltages, perform signal detection, and produce instrument data messages and housekeeping. SWIA has external connections to the spacecraft for cover actuation power, temperature sensors, and heater control, and to the Particles and Fields Data Processing Unit (PFDP) for instrument and attenuator power and digital clock/command/telemetry signals. Table 1 summarizes the main design parameters and performance of the flight instrument as built.

As shown in Fig. 2, SWIA mounts to a small platform at the $-Y/-X$ corner of the main deck of the spacecraft, with the symmetry axis of the analyzer aligned with the spacecraft

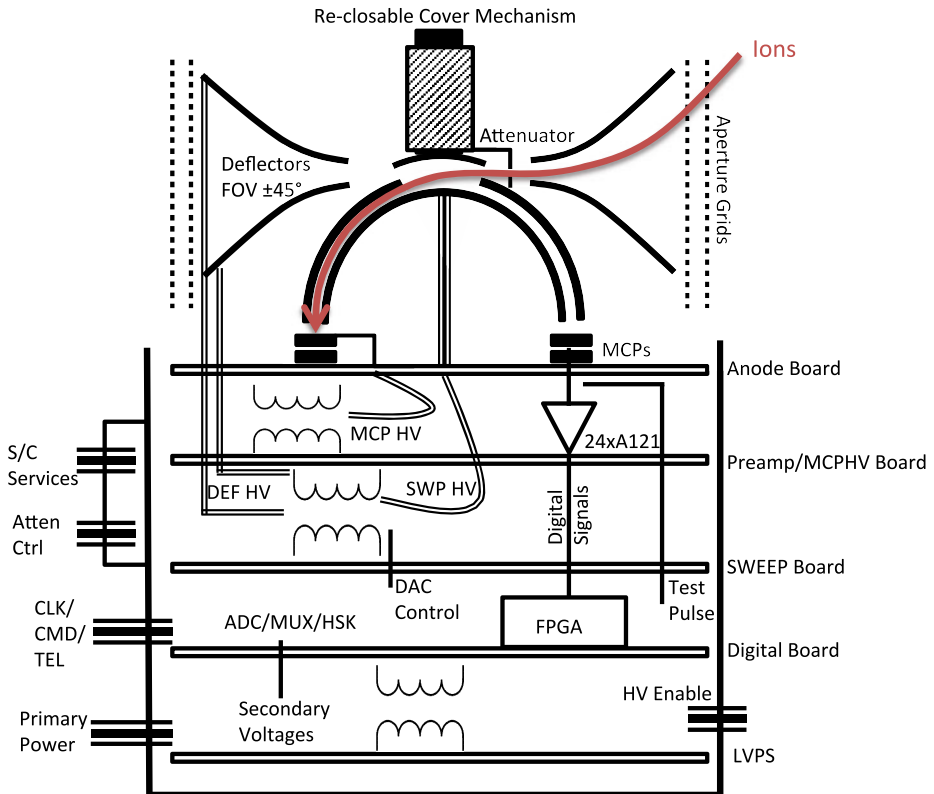


Fig. 1 Simplified block diagram of the SWIA instrument, showing the main analyzer components, the electronics boards and their primary functions, and external connections

Y -axis, at the same Z -coordinate as the solar panel hinge, providing a clear view of the $+Z$ and $-X$ hemispheres, as well as the portions of the $-Z$ and $+X$ hemispheres not blocked by the spacecraft body. The 360° (instrument phi angles) un-deflected field of view lies in the spacecraft X - Z plane, and the electrostatic deflectors steer this planar field of view $\pm 45^\circ$ out of this plane (instrument theta angles). The orientation of the analyzer was chosen to maximize coverage of the ion flow direction. For most science operations the Z -axis points to the sun, so the sensor has an unobstructed view of the solar wind. For the majority of operational attitudes, the X -axis points roughly toward nadir. In the sheath, we expect significant ion deflections, but the deflected flow vector should lie near the sun-nadir plane, close to the un-deflected field of view.

2.2 Design Considerations

The MAVEN mission design drove specific implementation choices for SWIA. As mentioned in Sect. 1.2, scientific requirements drove the design of the analyzer optics, detectors, and signal electronics. In addition to these constraints, the 3-axis stabilized platform and orbit around Mars drove the thermal design of the instrument, including deflector coatings (also constrained by the need to survive deep dips and exposure to atomic oxygen), radiator surfaces, thermal blanketing, and internal heat dissipation schemes. The requirements of the

Table 1 SWIA instrument performance

Parameter	Performance	Requirement	Comments
Resources	1.75 W, 2.62 kg, 22 × 16 × 14 cm ³		Sensor only, no blankets, PFDPDU converter efficiency not included
Analyzer Radii	R0 = 0.622 cm, R1 = 3.168 cm, R2 = 3.377 cm, R3 = 5.192 cm, R4 = 5.877 cm		R0 = Origin of toroidal section R1, R2 = Inner/outer hemisphere toroidal radii R3, R4 = Inner hemisphere/ top cap spherical radii
Analyzer constant	7.8		Measured
Deflector constant	6.4		Deflector/inner hemisphere voltage ratio for 45° deflection
Energy range	5.1 eV–26 keV	13 eV–5 keV	Nominal sweep, 96 steps
Analyzer energy resolution	14.5 %	15 %	Intrinsic
Binned energy resolution	9.4 % P0/P2 18.8 % P1		Nominal sweep
Accumulation Interval	1.7 ms		
Distribution Cadence	4 s	60 s	Sum or sample for lower rate to fit within available telemetry
Field of View	360° × 90° (360° × ±45°)	180° × 40°	Minus spacecraft obstructions Smaller for energies > 4.75 keV
Angular Resolution	22.5° × 22.5° P1 4.5° × 3.75° P2	30° (10° in sun direction)	Intrinsic theta resolution varies with deflection (see Fig. 3)
Geometric Factor	0.0056 cm ² sr eV/eV		Predicted: 360° analyzer X grid transmission X MCP efficiency
Attenuator	15		Full attenuation factor
Differential Energy Flux Range	10 ⁴ –7 × 10 ¹¹ eV/[eV cm ² s sr]	10 ⁷ –10 ¹⁰ eV/[eV cm ² s sr]	Count rates of a few Hz to 3 MHz, within A121 capability and above MCP background
Raw (P0) distribution	96 Energy × 24 Anode × 24 Defl.		Primarily a calibration product
Fine (P2) distribution	48E × 10A × 12D		Centered around peak rate Can sub-select 32E × 6A × 8D
Coarse (P1) distribution	48E × 16A × 4D		Fine anodes summed together Can bin to 24E or 16E
Energy spectra	48E		Sum over coarse product
Moments	n, V, P, Q		13 values, calculated onboard

spacecraft, the Electra relay package, and the science payload (particularly MAG and LPW) drove a design that minimized electromagnetic emissions, with no unshielded harnessing or exposed biased surfaces, and isolated instrument power services. The need to survive deep dips, in addition to constraining the thermal design, drove an instrument and PFDPDU design capable of a significant degree of autonomy, especially in regards to the high voltage operation.

2.3 Electrostatic Optics Design

SWIA shares an electrostatic optics design with STATIC. The toroidal analyzer design ensures that the average angle of incidence onto the MCPs is normal, eliminating any angular

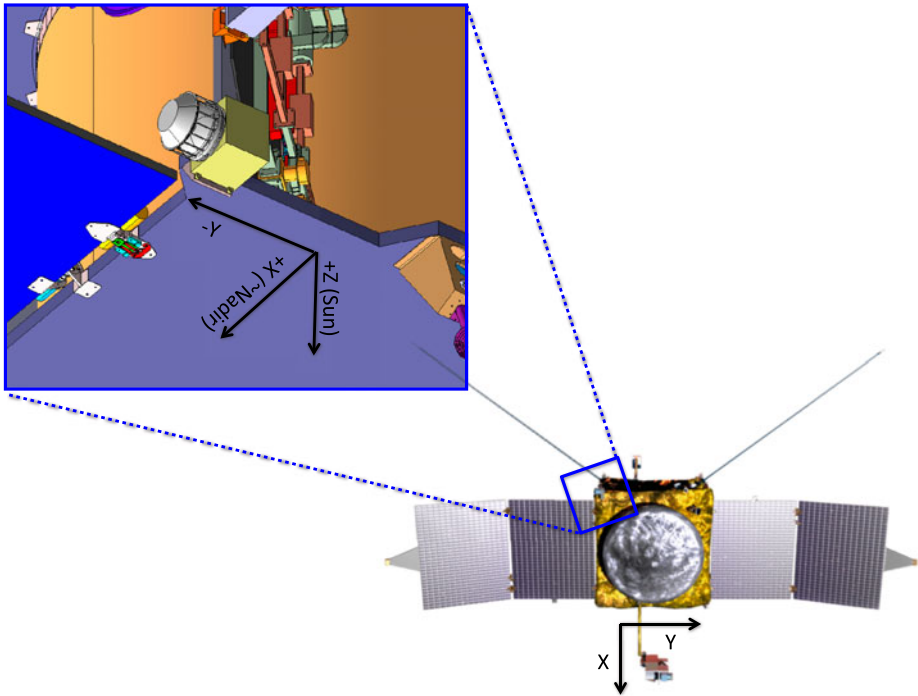


Fig. 2 Simplified view of the SWIA instrument accommodation on the MAVEN spacecraft, with spacecraft axes indicated

variation in sensitivity due to the convolution of a non-normal incidence angle and the MCP pore bias angle. In order to cover a broad angular range on a non-spinning platform, we utilize electrostatic deflectors, contained inside a pair of grounded aperture grids that screen the potential from the surrounding plasma and define the optics. To cover angles of $\pm 45^\circ$, we set the upper or lower deflector to a positive voltage up to 6.4 times larger than the inner hemisphere voltage (with the other deflector held at ground), to deflect incoming particles down or up. The deflectors operate with only positive voltages, in order to eliminate the emission and subsequent post-acceleration of photoelectrons that would perturb the local plasma environment. Therefore, the deflectors must “push” ions, rather than “pulling” as for an electron analyzer, resulting in somewhat lowered efficiency, since particles do not spend as much time in the strongest field region near the deflector. This forces a design trade between the desire to deflect as efficiently as possible (deflectors close together) and the desire to maximize sensitivity at all deflection angles (deflectors far apart, out of the optics path). The deflector design strikes a compromise between these extremes, utilizing a design that maintains good deflection efficiency (full 45° deflection up to 4.75 keV energies) with only a 50 % loss of sensitivity at the highest deflection angles.

The combination of analyzer and deflector voltages results in variable energy/angle response as a function of deflection angle, as shown in Fig. 3. For negative entrance theta angles, the deflector and analyzer bend incoming particles in opposite directions, resulting in overall angular focusing. In the other direction, the optics have more de-focusing properties (since both analyzer and deflector bend particles in the same direction, resulting in greater overall dispersion of ions with energy), as well as a more highly correlated energy/theta

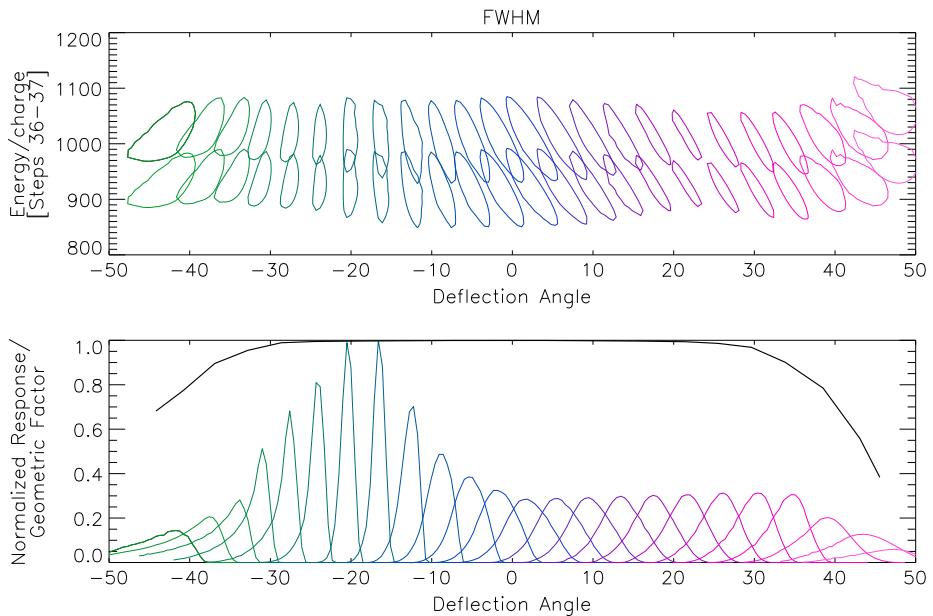


Fig. 3 Simulated SWIA analyzer response, as a function of energy and deflection angle. *Top panel* shows instrument energy/theta response for the 24 deflection steps, for two sample energies (*colored contours* indicate the full-width at half maximum response for each energy/deflection step), *bottom panel* shows normalized integrated theta response for each deflection step (*colored curves*) and overall instrument sensitivity (*black curve*)

response. Over the entire deflection range, the optics maintain better than 8° FWHM theta resolution. At deflection angles higher than $\sim \pm 25^\circ$, some ions that would otherwise reach the analyzer entrance instead impact the deflectors, reducing the overall sensitivity of the instrument. Only at deflection angles greater than $\sim +40^\circ$ does this loss significantly change the energy response of the sensor. The nominal energy/deflection sweep, shown in Fig. 3, ensures complete energy coverage, and full angular coverage of all but extremely narrow angular features.

A desire to measure even the most extreme solar wind fluxes without saturating the MCPs or electronics led to the decision to include a mechanical attenuator consisting of a “visor” with a slit that reduces the geometric factor by a factor of ~ 15 . The attenuator reduces sensitivity for a portion of the field of view around the nominal solar wind direction, as shown in Fig. 4, with complete attenuation for an instrument phi range of $\pm 30^\circ$, and partial attenuation up to $\pm 90^\circ$, ensuring that SWIA can measure the highest solar wind fluxes without saturating, while still maintaining some sensitivity to lower-flux populations such as pickup ions.

The SWIA optics design includes features that ensure a very low background from either photons or secondary particles. The deflectors have serrations with angles chosen to prevent any scattered ions from reaching the entrance to the analyzer. Meanwhile, the top cap surface and the inner surface of the outer hemisphere have scalloping that prevents scattered particles from reaching the detector, except after two or more reflections. Finally, all internal surfaces have a dendritic Ebanol-C coating, shown on THEMIS to essentially eliminate any signal from scattered photons (McFadden et al. 2008).

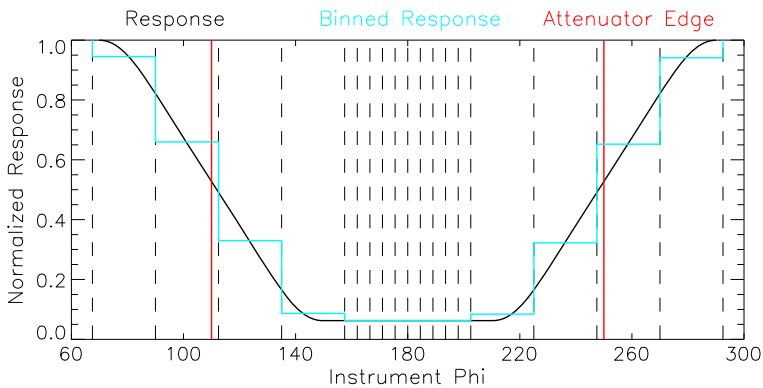


Fig. 4 Simulated SWIA analyzer sensitivity as a function of instrument phi, with attenuator closed, showing normalized intrinsic response as a function of phi angle (*black*) and binned by anode (*light blue*). *Dashed lines* indicate anode boundaries, and *red lines* show angular extent of attenuator

A final optics element, added to reduce the variation in sensitivity observed by the THEMIS ESA instruments at low energy (McFadden et al. 2008), is a second grounded grid between the analyzer exit and the MCPs. The presence of two grids, rather than the typical single grid, reduces the penetration of leakage fields from the MCP bias voltage into the exit region of the analyzer, ensuring constant sensitivity at even low particle energies.

The calculated analyzer geometric factor, together with predicted MCP efficiency and grid transmission, (see Table 1) implies full sensor count rates of 560 Hz–560 MHz (assuming isotropic fluxes, not the case in the solar wind) for differential energy fluxes of 10^5 – 10^{11} eV/[cm² s sr eV], the range of peak values expected from the magnetosphere up to cold dense solar wind. This corresponds to individual anode count rates ranging from 35 Hz to 7 MHz (utilizing large anodes for low fluxes, small anodes for the solar wind). At the low end, though we require some accumulation in time to acquire good statistics, count rates will remain well above background. At the high end, we will use the attenuator to lower the count rates to stay well within the 12 MHz capability of our preamplifiers.

2.4 Mechanical Design and Assembly

The SWIA instrument includes a number of sub-assemblies, some shown in Fig. 5 along with three views of the fully assembled flight instrument (sans thermal blankets). SWIA utilizes only materials and coatings appropriate for space, selected for their mechanical, thermal, and electrical properties, including aluminum for structure, bronze for standoffs between electronics boards, stainless steel for fasteners, and beryllium copper for grids, and PEEK for insulators. Coatings include Ebanol-C (copper black) on internal analyzer surfaces to prevent light scattering, black nickel (high-phosphor, non-magnetic) on the deflectors and aperture for its thermal properties, Z93 white paint on the radiator surface, Alodine to prevent oxidation of the main aluminum structure, and gold on many internal parts with conductivity requirements.

2.4.1 Analyzer Design and Assembly

Figure 6 shows a cutaway of the SWIA analyzer (almost entirely common with STATIC (McFadden et al. 2014)), including the top cover assembly, inner hemisphere/spider plate

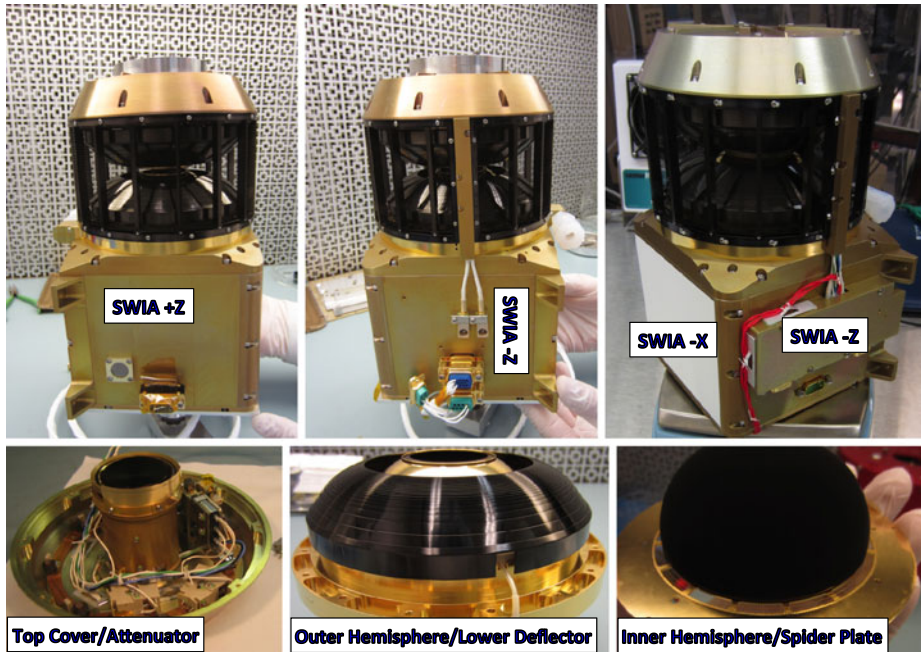


Fig. 5 Mechanical elements of the SWIA flight instrument. *Top three panels* show three different views of the instrument (un-blanketed), with (*upper right*) and without (*upper center*) the doghouse enclosure on the $-Z$ panel (spacecraft coordinates). *Bottom three panels* show top cover assembly (with attenuator mechanism), outer hemisphere/lower deflector assembly, and inner hemisphere/spider plate assembly

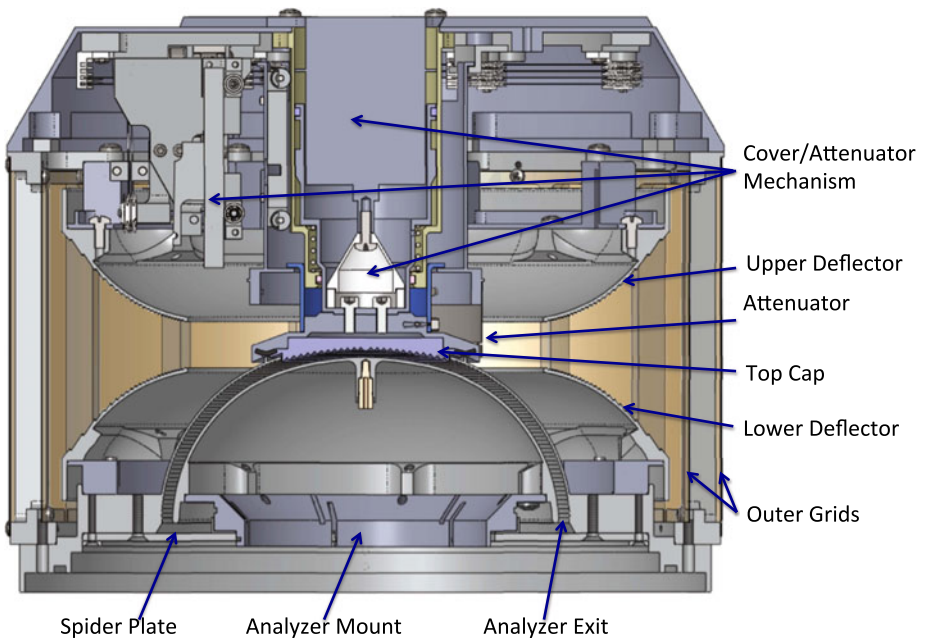


Fig. 6 A cutaway of the full SWIA/STATIC analyzer assembly (shown with cover and attenuator closed)

assembly, and the combined hemisphere/lower deflector assembly all shown individually in Fig. 5. For the electrostatic optics, the mounting of the two hemispheres must ensure very good concentricity to maintain consistent energy and angular resolution for all phi angles. We maintain concentricity by holding tight tolerances and minimizing the number of interfaces, and also by a unique design developed for previous UCB-SSL analyzers. The inner hemisphere and outer hemisphere both mount directly to the spider plate, the former through a zero-tolerance fit to an insulator with features that allow some compression, to maintain essentially perfect alignment between the inner hemisphere and spider plate. As described in Sect. 3, calibration data demonstrates that this design maintains the energy response to better than 2 % over the entire field of view of the instrument.

Above the hemisphere assembly, the top cover assembly mounts to the outer aperture assembly, with sixteen solid grid posts for structural support. The top cover assembly includes the attenuator mechanism, and a one-time (re-closeable on the ground) pin-puller cover mechanism that seals the analyzer and detector volume when closed, and holds the top cover fixed in the correct orientation to complete the electrostatic optics when open. Cover actuator power comes from the spacecraft, allowing us to open the cover in flight before powering the instrument. The cover mechanism also cages the mechanical attenuator when closed, both mechanically and electrically (via a cutoff switch).

2.4.2 Mechanical Attenuator

The mechanical attenuator (see Figs. 5 and 6) consists of a sliding cylinder outside of the top cap and cover mechanism that guides the attenuator (a small stainless steel sheet with a slit) in front of the sunward portion of the field of view when closed. The attenuator opens and closes with a mechanism utilizing shape memory alloy (SMA) wire to convert current to a mechanical stroke. End-of-travel switches, as well as a programmable software timeout, cut off current after actuation in order to prevent damage to the SMA. The mechanism is designed for bi-stability, in order to ensure that the unlikely case of a failure leaves the attenuator either fully open or fully closed. For MAVEN, this mechanism required long life (2000 cycles expected over the life of the mission) and a reproducible stroke, which took significant design effort and tuning to achieve. We tested a life test unit to >12,000 cycles, as well as actuating the mechanism over a full range of bus voltages and temperature in order to ensure reliability and reproducibility. Actuation takes between a few hundred milliseconds and just over a second for different temperature and bus voltage cases, and relaxation takes up to several minutes for the hottest case. In flight, we plan to utilize pulse durations of 750 ms, and a conservative time out between actuations of five minutes, in order to eliminate any risk of annealing the SMA wires.

2.4.3 MCP/Anode Board Assembly

The anode board performs a mix of electrical and mechanical functions. Mechanically, the main function of the assembly is to hold the microchannel plate detectors (MCPs) in place below the analyzer exit. These two 1 mm thick annuli are clamped, with no spacer between them, by treated and formed Be–Cu spring fingers held in compression by a set of inner and outer plastic clamps. An entrance grid with the same voltage as the front of the channel plate ensures that no stray voltages reach the front of the MCPs. The bias voltage for the front face of the MCPs routes through a tab to the spring fingers, from a press-fit pin that brings high voltage from the opposite side of the board. Two thin annular metallic rings sit below the MCP stack to make electrical contact between the board and the output face of

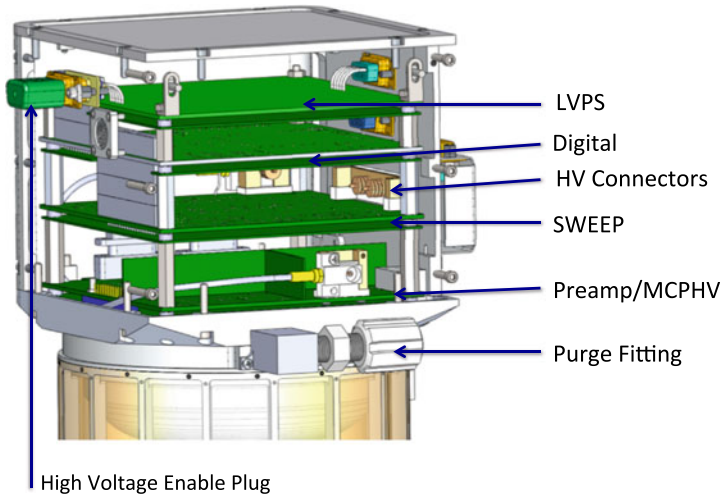


Fig. 7 A cutaway of the SWIA electronics box, from the $+X$ side (spacecraft coordinates), showing four of five electronics boards (anode hidden) and interconnections

the MCPs and keep them isolated from the anodes. This design, as opposed to the extra “cut-out” layer of circuit board utilized in the THEMIS/FAST design, simplified the anode layout significantly. The anode also serves as the mounting point for a high voltage tower that carries the sweep voltage to the inner hemisphere. The anode assembly connects to the outer hemisphere assembly above, and mounts to the transition plate at the top of the electronics box (see Fig. 7 for an external view, and Fig. 8 for a view of the anode assembly on the transition plate). The anode board has only filled through-holes (vias), in order to maintain a sealed volume around the detectors.

2.4.4 Contamination Control

As described above, SWIA has a cover (one-time opening on orbit, but re-closeable on the ground during testing) that seals the analyzer and detector volume, with the bottom of this volume established by the anode board, and a gasket between it and the outer hemisphere in order to reduce any leak paths. An external purge fitting (visible on the $+X$ side of the instrument in Fig. 5) enables a regulated quantity of purge gas to flow into the detector volume, passing through slits in the MCP mounting hardware and blowing over the detectors and out through the top cap, which acts as a spring-loaded poppet valve when closed. On MAVEN, instruments have T0 purge, with gas flowing until launch, maintaining instrument safety throughout spacecraft test and integration activities.

2.4.5 Electronics Box Assembly

From the transition plate, the other four electronics boards, with shield boards between each pair, stack on standoffs, as shown in Fig. 7. This design had a number of advantages for modular testing of different combinations of boards; however, it proved to have some disadvantages for heat conduction and mechanical stability. After some problems with shifts in the assembly (indicated by changes in fundamental frequencies) in vibration testing, the final flight design incorporated a number of board braces to better tie the stack of boards to the

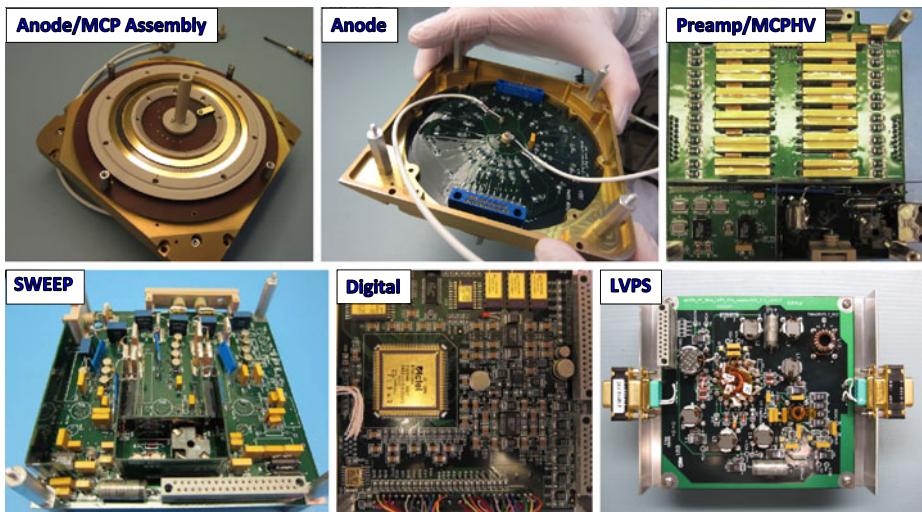


Fig. 8 The five SWIA flight instrument electronics boards. *Top left picture* shows the analyzer side of the anode board ($-Y$ side in spacecraft coordinates), mounted in the transition plate, with MCP stack and high voltage tower fully assembled. *Top center picture* shows the $+Y$ side of the anode board, mounted in the transition plate, with high voltage cables attached. Next four pictures show $+Y$ side of the other four electronics boards, in order from analyzer to bottom of electronics box

walls of the electronics box, as well as additional measures such as the use of high-strength fasteners and staking of fastener threads to gain additional strength.

Electrical connections between boards utilize several different schemes. External voltages and command/clock/telemetry signals come in to the LVPS and digital boards respectively on D-connectors to pigtailed on the boards (see Fig. 8). The LVPS also has a pigtail and D-connector to an external high-voltage enable plug. Other external connections route through the “dog-house” enclosure, but do not enter the main electronics box. Between boards, Airborne WTAX connectors route DAC outputs, housekeeping signals, and secondary voltages between the LVPS, digital, and sweep boards. MDM connectors on the preamp/MCPHV board connect to pigtailed on the digital board in order to route DAC outputs and secondary voltages to the MCPHV supply and bring signals from the preamplifiers to the digital board. Custom HV connectors route high voltages on coaxial cables to the two deflectors (through the dog-house and an enclosure along one of the aperture posts, blocking a small portion of the anti-sunward view), and the inner hemisphere and channel-plates via the anode board. Finally, Hypertronics KA-17 connectors carry charge pulses from the anode to the preamplifiers.

2.4.6 Thermal Design

Thermal considerations drove a number of aspects of the final SWIA mechanical design. The standoff-mounted electronics board stack had a number of issues related to the limited heat conduction path from the boards to the box walls. This necessitated the use of brass standoffs and a thermally conductive adhesive that increased conduction between the standoffs and ground pads in the corners of the electronics boards. The need for good thermal conduction also drove the addition of thick (at least 2 Oz. Cu) ground planes in all of the boards, directly tied to ground pads at all four corners and thereby to the standoffs and the electronics box. Though the original engineering model design had isolated grounds on each

board that could be connected or kept separate, the change to a single well-connected analog ground actually improved the electronic performance, and the flight instrument had no issues with electronic noise. The thick ground planes on the anode proved particularly useful for reducing crosstalk, in addition to ensuring a good thermal path for the channel plates and eliminating any concerns about thermal runaway. A transistor on the MCPHV supply that dissipated a large amount of power utilized an additional heat sink to the box wall to dissipate heat.

The exterior of the instrument (originally thermally decoupled from the bus, but later changed to a coupled design) utilized a variety of thermal treatments to maintain the electronics box below 50 °C for hot cases (particularly cruise phase) and minimize the need for heater power in cold cases (particularly eclipses). Exterior aperture and grid parts, as well as deflector surfaces, utilized Black Nickel for its high absorptivity/emissivity ratio. The remainder of the instrument has multi-layer insulation thermal blankets, with the exception of the $-X$ panel, which has a radiator surface painted with Z93 white paint with a very low absorptivity/emissivity ratio.

2.5 Electronics Design and Operation

2.5.1 Anode Board

The anode board, as described in Sect. 2.4.3, houses a chevron pair of annular microchannel plate detectors. The MCPs, with a high voltage of 1.5–2.5 kV across them, produce secondary electron cascades in response to incoming ions, yielding pulses of $\sim 2 \times 10^6$ electrons. The SWIA flight plates, supplied by Photonis, have pores with a 40:1 depth/diameter ratio, and have a total stack resistance of 17.3 Mohms (at room temperature). This low resistance corresponds to a high strip recharge current that allows the sensor to count at a high rate on the order of 500 kHz (higher for brief periods) before significant saturation (MCP droop) occurs. Since the solar wind is only observed for a brief period of the energy/deflector sweep pattern, and the attenuator limits instrument sensitivity in the sun direction, MCP droop should not affect the sensor in normal operation. A 330 k Ω resistor between the output face of the channel plates and ground produces a post-acceleration voltage of ~ 50 V and prevents the charge cloud from spreading too much between the MCPs and the anode.

Metallized anode pads collect the charge pulses and route them to discrete preamplifiers on the next board. The anode pattern covers the entire annulus under the MCPs, with ten 4.5° anodes covering the portion of the detector that responds to the nominal solar wind direction, and an additional fourteen 22.5° anodes covering the remainder. Each anode has a ~ 1 M Ω resistor to ground to bleed off DC charge accumulation, and a 50 Ω resistor in series to the connector to the preamplifier board. In order to reduce noise and crosstalk, anodes are separated from traces on the opposite side of the board by two ground planes, and adjacent traces have ground traces separating them from each other and from the high voltage connections (visible in Fig. 8).

High voltage for the inner hemisphere and channel plate runs on coaxial cables from the respective supplies to the anode board. The coax sheaths solder to ground pads on the board, and center conductors connect to the high voltage tower and through a pin and tab to the front face of the MCPs. High voltage return and analog ground connect on the board (and to chassis ground). This did not result in any issues with signal integrity; however, to eliminate noise, we found it critical that high voltage return also connect to analog ground at the supply, allowing current to return to the supply.

The SWIA anode has many similarities to the THEMIS and FAST ESA anodes (Carlson et al. 2001; McFadden et al. 2008), with a few key exceptions. As described above, metal

support rings rather than a recessed layer serve to isolate the anodes from the MCP output face. In addition, we moved clamp diodes (to provide protection to the preamplifiers in the event of a high voltage discharge) from the anode to the preamplifier board. This simplified the anode layout considerably, and placed the diodes closer to the components needing their protection.

2.5.2 Preamp/MCPHV Board

Charge pulses from the anodes travel on Hypertronics KA-17 connectors to the next board, which contains 24 Amptek A121 charge-sensitive preamplifiers. The signals capacitively couple to the inputs of the preamplifiers, which have a programmable threshold controlled by DAC outputs from the FPGA on the digital board. We tune the A121's with external resistors to produce an output pulse with a width of 50 ns, and to have a well-characterized fixed dead time of 100 ns (allowing count rates of up to 10 MHz periodic for each signal chain). Digital output pulses travel on MDM connectors to pigtailed on the digital board, and ultimately to ripple counters in the FPGA. We use a test pulse generated by the FPGA to test the detection electronics without high voltage enabled. A counter divides the digitally produced test pulse signal down into four different frequencies, capacitively coupled to individual signal chains, such that adjacent anodes do not share the same frequency (enabling testing for crosstalk).

A high voltage supply for the MCPs also resides on this board (separated by a shield wall—see Fig. 8). This supply utilizes a self-resonant topology to produce a negative voltage of up to -2.5 kV (applied to the input face of the channel plates). A DAC output from the digital board controls the output of the supply. The supply drives a significant resistive load (~ 2 kV across ~ 17.3 Mohms at room temperature), so we heat-sink the transistors to the transition plate to dissipate any heat buildup on the board. High voltage control lines and read-backs share the same MDM connectors with the preamplifier output signals.

2.5.3 Sweep Board

The sweep board has a single bi-polar raw high voltage supply, utilizing a self-resonant design, and operates at a nominal voltage of ± 4.2 kV (equal and opposite). Optically coupled high voltage outputs provide the inner hemisphere (negative) and the deflector (positive) high voltages, each with a range of 0–4 kV in magnitude. These high voltages pass from the sweep board to their respective destinations through custom connectors and coaxial cables, with high voltage returns connected at the sweep board so any currents can close. DAC outputs from the digital board control the raw supply and the outputs. The sweep board represents a near copy of the STATIC sweep board, and incorporates the same circuitry to measure the outputs of op-amps in the control feedback loop; however, SWIA does not incorporate the capability to correct for offsets as STATIC does. SWIA, which has much less stringent low energy requirements than STATIC, does not require this corrective capability. SWIA does incorporate the same low-drift op-amps as STATIC in the control and feedback loop, ensuring very good stability even without offset circuitry.

2.5.4 Digital Board and FPGA

The digital board contains an FPGA that controls the high voltage sweep, accumulates counts, produces data products, produces the test pulse signal that goes to the preamplifier board, calculates check sums for the sweep tables, multiplexes and converts housekeeping values for all of the secondary and high voltages (as well as two thermistors), and interfaces

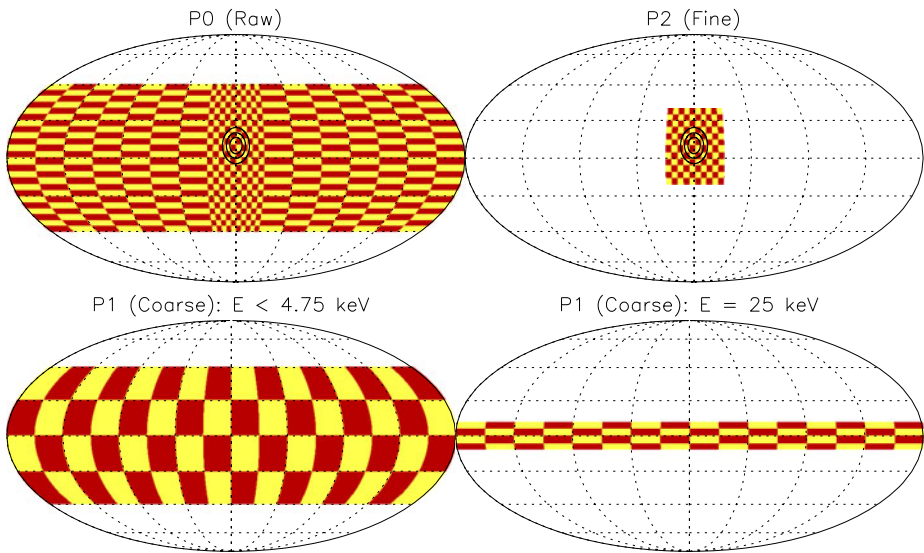


Fig. 9 Angular coverage and resolution of SWIA ion velocity distributions (Mollweide projection), for raw (P0, large data volume, primarily a calibration product), fine (P2, primarily for solar wind—contours show a typical solar wind distribution), and coarse (P1, for magnetosphere and pickup ions) products. Two angular plots for P1 show the energy dependence of the angles covered by the deflectors, with full theta angle coverage up to 4.75 keV (well above nominal solar wind energies), and proportionally reduced coverage at higher ion energies

with the PFDPU. The digital board connects to the SWEEP board and the LVPS with WTAX connectors, and to the preamplifier board with MDM pigtailed. Digital and analog grounds connect on the board, with analog ground directly connected to chassis, but digital ground otherwise isolated.

Digital signals from the 24 A121 preamplifiers, after conversion to a 3.3 volt input level, accumulate in ripple counters over 1.7 ms accumulation intervals, for each of the 96 energy steps \times 24 deflector steps in the sweep. Short ~ 1 ms dead times at the end of each energy step (every 24 accumulation intervals), and a longer ~ 21.5 ms dead time at the end of the cycle (every 2304 accumulation intervals), ensure that we do not accumulate counts during high voltage retraces. The overall duty cycle is $\sim 98\%$. The FPGA produces three data products from these accumulations, with angular coverage and resolution (for a nominal voltage sweep) as shown in Fig. 9. The first product, P0 (Raw), consists of the 24 raw anode counts for each of the accumulation intervals, resulting in a $96 \times 24 \times 24$ array. The P1 (Coarse) product sums over the ten small anodes in two groups to produce a total of sixteen 22.5 degree anode bins, sums over groups of 6 deflection steps to produce 4 deflection bins, and sums over adjacent energy steps to produce 48 energy bins. The P2 (Fine) product finds the peak count rate in the ten small anodes, and sends back counts for 48 energy steps and 12 deflection steps containing the peak (with the framing around the peak programmable). The SWIA FPGA sends P0, P1, and P2 to the PFDPU in the form of small messages of a few tens of words. Given the formidable size of P0, we typically rely on P1 and P2 for the main science outputs, with P2 utilized to measure the very localized intense solar wind flux, and P1 utilized to measure the more thermalized fluxes in the Martian magnetosphere (as well as pickup ions).

The FPGA also controls DACs that set all high voltage levels and preamplifier thresholds. High voltage controls can either utilize a sweep table stored in SRAM, or can operate in diagnostic mode. Control circuitry utilizes 16-bit AD5544 current-mode DACs with a current-to-voltage op-amp stage to achieve high precision. High voltage controls utilize multiple DACs chained together to achieve high dynamic range and resolution. The secondary 28 analog voltage that powers the high voltage supplies passes through a FET switch, only opened after receipt of two “key codes” entered in succession (see Sect. 4.1.2), preventing accidental high voltage operation in air.

2.5.5 Low Voltage Power Converter

The LVPS produces secondary digital voltages of 2.5, 3.3, and 5 volts, and secondary analog voltages of -5 , $+5$, 12, and 28 volts. All secondary voltages are isolated from the regulated primary 28-volt input from the PFDPU, and secondary returns connect to chassis. The secondary 28-volt analog service that powers the high voltage supplies passes through an enable plug before reaching the digital board, as an additional safeguard against accidental high voltage operation.

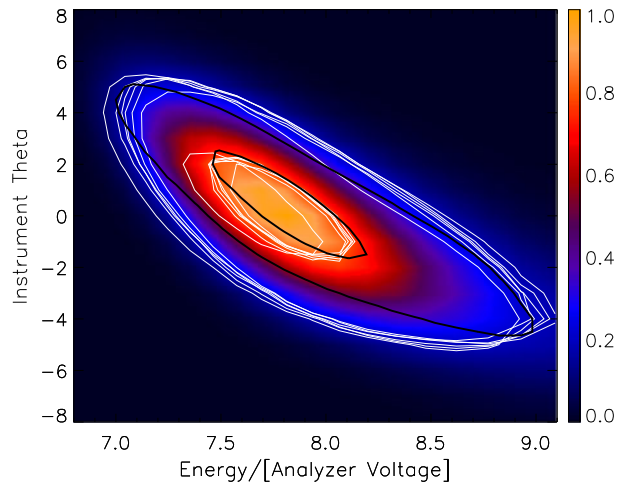
3 SWIA Testing and Calibration

The SWIA flight instrument went through a rigorous qualification program, starting with board-level testing, proceeding through instrument-level testing, and culminating at observatory-level testing once integrated to the spacecraft. Environmental testing at both the instrument and observatory level included magnetics screening, electromagnetic emissions and compatibility, vibration, and thermal vacuum.

After the completion of environmental testing, we performed a complete calibration of the sensor. The UCB/SSL calibration facility, newly improved for MAVEN, consists of a vacuum chamber with electron and ion sources, Helmholtz coils to null external fields (more important for electron sensors), and a 3-axis manipulator to expose different portions of the instrument field of view to a particle source. Using this facility, with an electron-impact ion source that ionizes residual gas in the chamber, we performed scans over the full instrument phi range (anode angles), over an energy range of 10 eV–5 keV, and over the full theta range (deflection angles). We performed translational scans across the aperture at a variety of different deflection angles. We performed a large number of high-resolution two-dimensional energy-theta scans for different phi and theta angles, and at multiple energies. We conducted tests with the attenuator both open and closed. In addition, we exposed the instrument to a range of fluxes sufficient to verify the sensitivity requirements. Finally, we scanned the MCP pulse height distribution by varying the preamplifier thresholds. All calibration data corresponded well to simulation outputs, validating the precise mechanical design and assembly of the instrument.

Figure 10 shows perhaps the most important calibration product, a series of energy-deflection angle scans at six equally spaced phi angles (and zero deflection). The close correspondence of the six scans demonstrates the high concentricity of the two hemispheres, good to a few percent or better around the entire aperture (a tolerance of better than 40 μm , or 0.0016"). The correspondence between measurement and simulation (same as zero deflection case in Fig. 3) demonstrates that the analyzer was fabricated and assembled precisely according to the specifications from the optics simulation. Slight ($\sim 1^\circ$) theta-angle broadening in the measured response results from the non-zero angular width of the ion calibration beam; however, this slight broadening effect does not significantly affect the overall

Fig. 10 Measured energy/deflection angle response of the SWIA flight instrument. Colors show average energy/theta response for six evenly spaced phi angles. *White contours* show 20 % and 80 % levels for each of the six phi angles. *Black curves* show simulated 20 % and 80 % level contours. Slight angular broadening of the calibration data as compared to simulation results primarily from the ~ 1 degree angular width of the calibration ion beam



measured integrated energy or theta response, which match simulation perfectly. Analogous results at non-zero deflection angles show a similarly high degree of correspondence, validating the fabrication and assembly of the deflectors.

Figure 11 shows another important calibration product, phi scans with the attenuator open and closed (at zero deflection). With the attenuator out, the instrument has nearly uniform sensitivity as a function of phi angle, with the exception of small dips in the response at the position of ribs in the spider plate at the analyzer exit, and a slightly larger dip in sensitivity on the anti-sunward side of the analyzer ($\phi = 0$) where the attenuator and cover power routes through a small enclosure and blocks a portion of the aperture. We also note a slight increase in the effective geometric factor around the small anodes, which results from a small degree of double counting of pulses due to the spread in the charge cloud from the output face of the MCP to the anode (this slightly increased geometric factor can be easily compensated for in ground software). Beyond these effects, we find almost perfectly uniform sensitivity, once again indicating very good hemisphere concentricity, but also uniform detector response. The bottom panel of Fig. 11 shows the same product, but with attenuator closed. The ratio of these two curves corresponds quite well to the simulation results in Fig. 4 for a fixed energy and deflection angle, validating the fabrication, assembly, and actuation of the mechanical attenuator.

4 SWIA Operation

4.1 PFDPU Flight Software Functions

In many respects, SWIA can operate as a nearly stand-alone instrument. With internal memory to store lookup tables and a very capable FPGA, SWIA can operate semi-autonomously, sweeping its own high voltage, and producing data products. Despite this high level of intrinsic capability, SWIA relies on the Particle and Fields Data Processing Unit (PFDPU) for a number of functions, including primary instrument and attenuator power, fault protection, mode control, some data processing, and communication with the spacecraft processor and thus the ground.

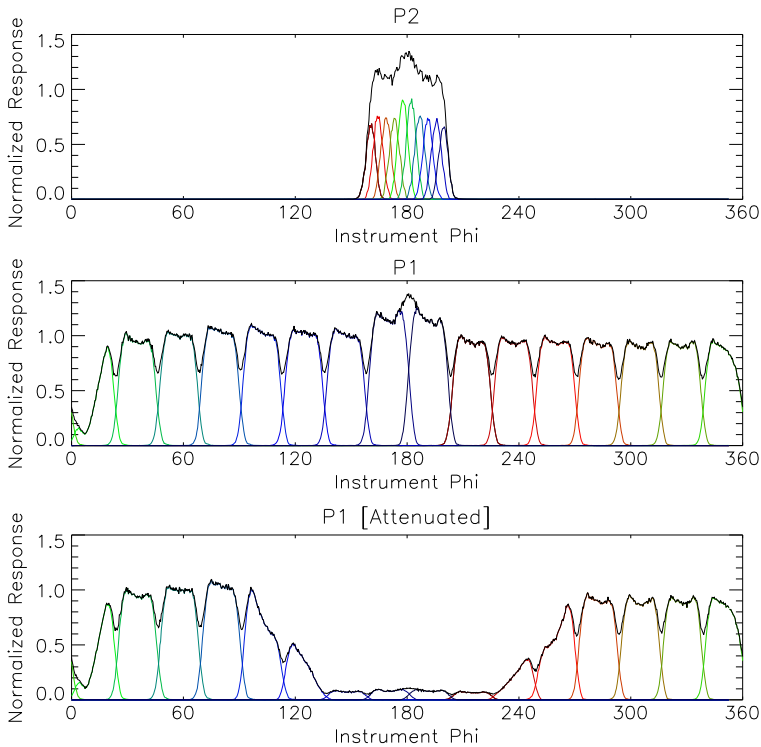


Fig. 11 Measured phi response of the SWIA flight instrument, for each anode (*colored curves*) and overall (*black curves*). Top panel shows counts in the small anodes (fine resolution, P2 product). *Bottom two panels* show counts in the large anodes (P1 product), including small anode counts summed into two bins, with attenuator open and closed. Dips in sensitivity at anode boundaries result from ribs in the spider plate at the analyzer exit. The increase in sensitivity around $\Phi = 180$, where no rib exists (to ensure maximum sensitivity to solar wind ions), results from moderate levels of double counting due to the spread in the charge cloud between the exit face of the MCP and the anode

4.1.1 Data Processing

The PFDPU accumulates messages (a few words to a few tens of words in length) from SWIA in order to build up full data products. For SWIA, these messages include the three data products described in Sect. 2.5.4, including P0 (though we typically do not enable this calibration product in flight), P1, and P2, and also housekeeping (HSK) and memory diagnostic (LUT) messages. These messages accumulate into direct memory access buffers that switch every second, with four such readouts serving to build up a full 4-second message from SWIA. The flight software then utilizes ground-programmable options to determine how often to send a packet of a particular type, and what binning and decimation to use. For P1 (coarse distributions), we can send the product at full resolution (48 energies), or at a binned energy resolution 2 or 3 times lower (24 or 16 energies). For P2 (fine distributions), we can send either the full $48 \times 12 \times 10$ product, or a $32 \times 8 \times 6$ subset thereof. For each type, we can form packets at any interval 4×2^N seconds, with N programmable. Since P2 moves in phase space to follow the peak, we only sample in time. For P1, we can sum or sample the distributions over the 4×2^N interval.

In addition to summing, sampling, and binning as needed for coarse and fine distributions, flight software computes moments and energy spectra from the distributions. Moment calculations can utilize either P1 or P2 data (using separate tables of coefficients—see Sect. 4.1.4), allowing high cadence measurements of the bulk properties of the distribution in either the solar wind or the sheath. To calculate energy spectra, we sum over all angular bins of the coarse P1 distributions. Since a simple sum does not account for the variation in geometric factor over the field of view, one should not use the spectra for quantitative calculations; nonetheless, they represent an extremely useful high-cadence diagnostic, which consumes little telemetry.

The PFDPU flight software packages each data product (Raw, Coarse, Fine, Moment, Spectra, Housekeeping) into CCSDS packets, with each packet including timing and other ancillary information such as attenuator status, science mode, compression type, etc. in addition to science or housekeeping data. The number of products per packet for SWIA ranges from 16 for Moment and Spectra telemetry, to 1/6 for Coarse distribution telemetry with the highest energy resolution. For Coarse and Fine 3d products, the software produces two separate streams of packets with different programmable sampling intervals, termed Archive and Survey. The Survey packets are transferred directly to the spacecraft, and nominally all reach the ground (with sampling intervals chosen to fit into a constrained data volume). The Archive packets, accumulated into a circular buffer with a two-week capacity in flash memory in the PFDPU, have a smaller sampling interval and correspondingly higher telemetry rates. By utilizing the Survey stream on the ground, scientists can choose small portions of Archive memory to download, allowing investigation of selected time periods with much higher cadence data.

The PFDPU applies two levels of compression to the SWIA science data. First, it compresses all counts to 8 bits, using a lossy log compression scheme that maintains $\sim 6\%$ resolution in count rate. Next, the software applies packet compression, using a lossless Huffman-encoding scheme, to all science data at the packet level. This produces a variable telemetry rate, depending on count rate and other factors (low count rates and uniform count rates compress efficiently). In order to maximize usage of available telemetry, we size the Survey volume such that uncompressed packets fill the nominal allocation, and then utilize extra telemetry volume resulting from packet compression to send Archive data.

4.1.2 Fault Protection and High Voltage Control

The PFDPU also handles fault protection and high voltage control for SWIA. The software loads sweep lookup tables of high voltage DAC values, stored in the EEPROM, to the instrument SRAM upon power-on. It also monitors the checksums of these tables and reloads if they do not match the expected values. The PFDPU controls when the high voltage can power on, utilizing an arm bit enabled or disabled by ground control, or by fault protection on the spacecraft (“Zone Alerts”). When enabled, the PFDPU monitors the state of the SWIA high voltage and ramps it up when allowed. Similarly, when disabled, it shuts the SWIA high voltage off if it sees a voltage over a nominal value of ~ 100 V in the housekeeping. This scheme gives the suite a high degree of autonomy, since no ground command is required to turn the instrument on or off and ramp the high voltage up or down. If the spacecraft issues a Zone Alert for high pressure (in a deep dip, for example), or if the Zone Alert signal disappears entirely due to a spacecraft fault, the PFDPU will autonomously send commands to ramp down SWIA’s high voltage. When the Zone Alert clears, the PFDPU will autonomously send commands to bring SWIA’s high voltage back up and begin normal science operation.

This scheme allows for the highest return of science data with the least amount of ground intervention. However, it does complicate ground testing, especially for non-vacuum conditions. To guard against this, we rely on the high voltage enable plug described in Sect. 2.5.4, and the key-codes described in Sect. 2.5.5. For most ground testing, the PFDPU does not contain the correct key codes to turn on the SWIA high voltage, even if the arm bit should accidentally get enabled. In addition, the PFDPU monitors the cover status, and does not allow high voltage operation with it closed.

4.1.3 Attenuator Control and Mode Switching

The PFDPU also controls SWIA's mechanical attenuator. If enabled, the software monitors the peak count rate recorded in the P2 data product, and applies power to move the attenuator in or out in response to count rates over or under programmable thresholds. Attenuator actuations can only occur subject to an enable bit, with a programmable hardware actuation timeout (nominally 5 minutes), a programmable minimum interval between actuations (4×2^N seconds), and a programmable maximum number of actuations between resets. In order to prevent rapid in and out actuations ("shuttering") of the attenuator, we typically set the minimum interval between actuations to a large value of $N = 7$, or 512 seconds.

Similarly, the flight software controls the telemetry mode of the instrument. The mode does not represent a difference in the operation of the hardware; rather, it simply represents a difference in the mix of telemetry sent to the Survey and Archive streams (see Sect. 4.2). In order to determine when to switch between "Solar Wind Mode" and "Sheath Mode" (see Sect. 4.2), the software monitors the ratio between the total number of counts contained in the P1 product and the P2 product, switching to the former if P2 contains most of the counts (a narrow distribution), and to the latter if P1 contains many counts not in P2 (a more spread-out distribution). This mode control utilizes programmable thresholds, and occurs subject to a programmable minimum interval between mode changes (4×2^N seconds). As for the attenuator control, we typically set $N = 7$, corresponding to at least 512 seconds between mode changes.

4.1.4 Onboard Moment Computation

The computation of moments represents the most significant task that the PFDPU flight software performs for SWIA (indeed, this has the largest computational burden of any single software task the PFDPU performs). For every 4-second accumulation, the software computes the bulk moments: n (density, one value), \mathbf{V} (velocity, three values), \mathbf{P} (pressure, six values), \mathbf{Q} (heat flux, three values). In Solar Wind mode, the moment computation utilizes the P2 product, while in Sheath mode it utilizes the P1 product. The two calculations, using direct integration (approximated by weighted sums of counts) to compute the moments of the distribution, utilize different sets of coefficients, each including all angle and energy factors, as well as the variation in geometric factor over the field of view. The coefficient tables implicitly depend on the sweep table, necessitating a reload if the sweep table changes. The onboard moment calculation assumes 100 % protons. In the solar wind the small alpha particle population introduces an error on the order of $n_\alpha / (\sqrt{2}n_p)$ in the moments, typically on the order of 3 % (density too low, velocity too high). In the heavy ion-dominated Martian magnetosphere, much larger errors can result.

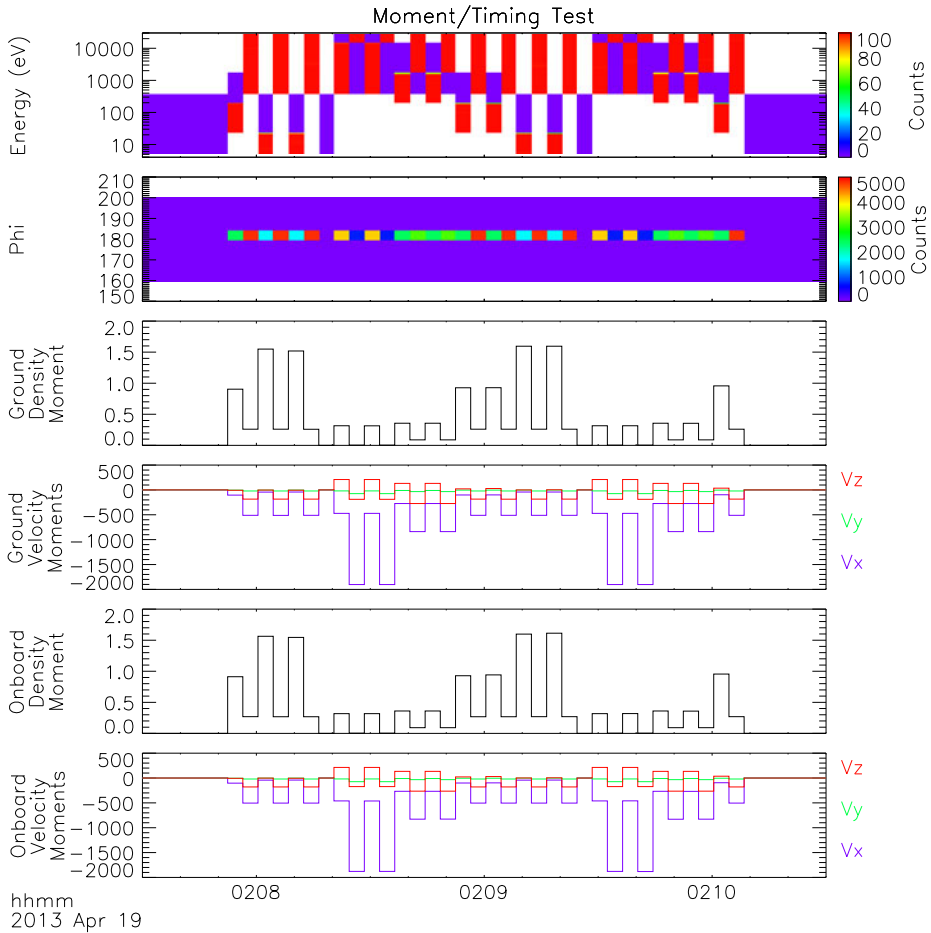


Fig. 12 Fine distribution data from a test conducted with the SWIA engineering model and the PFDPU, utilizing an external stimulus connected directly to one of the digital counter inputs to the FPGA. The results confirm the product timing to a few milliseconds, and validate the onboard fine distribution moment computation performed by flight software against moments computed “on the ground” from the full 3d distribution

The moment computation for Solar Wind mode proves particularly challenging, since the software must select a subset of a large coefficient table, appropriately indexed for the portion of the energy/angle map chosen by the SWIA FPGA (based upon the location of the peak count rate, and the parameters that determine the framing of the P2 product around that peak). Getting this computation correct required significant testing and iteration of the algorithm and coefficients. Figure 12 shows the results of a ground test utilized to validate the software moment computation and verify product timing. This extremely valuable test employed an external digital stimulus directly fed to the SWIA EM digital board, allowing injection of a periodic train of pulses with known timing. By comparing the onboard calculation to an independent calculation of the moments from the full 3-d data, using 4-second pulse trains injected with various phasing relative to the SWIA 4-second cycle, we validated all aspects of the moment computation.

4.2 Modes, Telemetry Rates, and Archiving

SWIA has a nominal telemetry allocation of 604 bps for all science and housekeeping data. At some points in the mission, higher downlink capability enabled by smaller Earth-Mars distances will permit a larger data rate (up to 3.25 times higher during the nominal mission). As described in Sect. 4.1.1, we size Survey telemetry to utilize as much as possible of the nominal allocation, and use any extra capacity, in addition to that gained by packet compression of Survey data, to send selected Archive telemetry (also compressed), with the amount of Archive return determined by the variable compression efficiency. In general, we cannot exactly fill the allocation, or match the rates for Solar Wind and Sheath modes, so we size all rates such that the orbit average cannot exceed our allocation. Table 2 shows telemetry for the two modes, for sample allocations that may apply during different portions of the mission. We can also adjust the mix of data products as needed to focus on different science priorities, by choosing higher energy/angle resolution at the expense of lower time resolution, as shown for the “High-Angle Low-Time” mode. In Solar Wind mode we send primarily fine distributions, with a smattering of coarse distributions to allow us to see pickup ions. In Sheath mode, we typically only send coarse distributions. For both modes, we send spectra and moments, to provide a high cadence view of the bulk proton properties.

Meanwhile, for all phases of the mission, we plan to send high resolution 3d data to Archive memory at a fixed rate, as shown in the bottom two rows of Table 2. As described in Sect. 4.1.1, by utilizing the additional capability gained from compressing Survey data, we can downlink selected portions of this data, with the percentage of Archive return varying with downlink capability and compression efficiency.

All data products shown in Table 2 will be archived in the Planetary Data System. Every SWIA packet (including science telemetry and housekeeping) will be archived in two files per UT day (one for Survey, one for Archive) containing all Particles and Fields APIDs in their original compressed binary format (Level 0). Coarse and fine 3d distributions, as well as onboard moments and spectra, will be calibrated to reflect all variations in instrument sensitivity, converted to physical units, and archived in six files per UT day (coarse and fine survey and archive data, and onboard survey moments and energy spectra). We will also make all data reduction and analysis software (including software that can compute “ground moments” from the 3d data) publicly available for use by the community.

4.3 Commanding

The SWIA instrument can be commanded in several different ways. First, we can command the instrument FPGA directly using a CDI (Command and Data Interface) protocol to do memory operations (loading lookup tables and selecting the active table) and memory tests, control high voltage in both sweeping and diagnostic modes, enable and disable housekeeping and science messages, control the test pulser, set preamplifier thresholds, and set parameters that control the framing of the P2 product and allow the masking of noisy anodes. Using an additional set of flight software commands, we can call functions that power the instrument on and off, load lookup tables, enable and disable high voltage and automatic attenuator control, ramp high voltage, request fast housekeeping packets, and play back archive data. The flight software functions themselves can utilize the CDI commands, and in fact supersede CDI commands for loading lookup tables and controlling high voltage from the ground.

A third type of “command” is an RTS, or Real Time Sequence, which consists of a list of CDI commands and/or flight software function calls pre-loaded in the EEPROM and capable

Table 2 Sample survey and archive telemetry

Product (Size including packet headers)	Coarse	Fine (Short bytes, Long bytes)	Spectra (784 bytes for 16 spectra)	Moments (432 bytes for 16 sets)	House-keeping (108 bytes)	Total Data Rate (bits per sec)
1 × Solar Wind Survey	Med every 128 s (99 bps)	Short every 32 s (388 bps)	8 s cadence (50 bps)	4 s cadence (54 bps)	64 s cadence (13.5 bps)	604.5 bps
1 × Sheath Survey	Med 32 s (396 bps)	None	8 s (50 bps)	4 s (54 bps)	64 s (13.5 bps)	513.5 bps
High-Angle Low-Time 1 × Solar Wind Survey	Full 256 s (99 bps)	Long 128 s (363 bps)	8 s (50 bps)	4 s (54 bps)	64 s (13.5 bps)	579.5 bps
High-Angle Low-Time 1 × Sheath Survey	Full 64 s (396 bps)	None	8 s (50 bps)	4 s (54 bps)	64 s (13.5 bps)	513.5 bps
1.5 × Solar Wind Survey	Med 256 s (49.5 bps)	Short 16 s (776 bps)	8 s (50 bps)	4 s (54 bps)	64 s (13.5 bps)	943 bps
1.5 × Sheath Survey	Med 16 s (792 bps)	None	8 s (50 bps)	4 s (54 bps)	64 s (13.5 bps)	909.5 bps
2 × Solar Wind Survey	Med 64 s (198 bps)	Short 16 s (776 bps)	4 s (100 bps)	4 s (54 bps)	64 s (13.5 bps)	1141.5 bps
2 × Sheath Survey	Med 16 s (792 bps)	None	4 s (100 bps)	4 s (54 bps)	64 s (13.5 bps)	959.5 bps
3.25 × Solar Wind Survey	Med 64 s (198 bps)	Short 8 s (1552 bps)	4 s (100 bps)	4 s (54 bps)	64 s (13.5 bps)	1917.5 bps
3.25 × Sheath Survey	Med 8 s (1584 bps)	None	4 s (100 bps)	4 s (54 bps)	64 s (13.5 bps)	1751.5 bps
Nominal Solar Wind Archive	Full 32 s (792 bps)	Long 8 s (5808 bps)	None	None	None	6600 bps to Archive
Nominal Sheath Archive	Full 8 s (3168 bps)	None	None	None	None	3168 bps to Archive

of executing on board. The PFDPU uses RTS calls to power on and off the SWIA instrument, turn on and off high voltage, and put the instrument in Solar Wind or Sheath mode (therefore, changing telemetry rates requires a reload of the RTS block in the EEPROM). RTSs can and do call each other, and multiple RTSs can operate simultaneously. RTSs can be individually enabled and disabled, and run from the ground or in response to a spacecraft command or fault protection event. As described in Sect. 4.1.2, this allows the instrument suite to operate with a high degree of autonomy if desired.

4.4 Known Operational Limitations

The SWIA instrument has some known operational limitations that one should keep in mind when using the data. First and foremost, SWIA lacks mass discrimination capability. SWIA measures differential energy fluxes, independent of ion species, with no systematic errors anticipated in this measurement. However, converting these measured fluxes to distribution functions, or calculating bulk moments, requires an assumption about the composition. Given the assumption of $M = 1$, a calculation of the first two moments for a heavy ion distribution will result in errors of \sqrt{M} (density too low, and velocity too high). Therefore, SWIA measurements will typically not provide accurate moments inside the heavy ion-dominated Martian magnetosphere. Using STATIC data, we can correct some of our data for these effects, but in regions with no overlap in energy and/or field of view any corrections will have to rely on assumptions.

SWIA's incomplete field of view and energy range also limit the accuracy of ion moments in some environments. In the solar wind, the field of view and energy range will always cover the vast majority of the distribution and moments should prove fairly accurate; however, in the magnetosphere, where the ion population slows and thermalizes sufficiently, incomplete coverage of the distribution can often result in significant errors. The most significant errors will occur for cases with ion energies at or below the lowest energy measured (~ 5 eV for a nominal sweep) or for distributions with thermal velocity comparable to or larger than bulk velocity (implying a significant portion of the distribution outside of the field of view). We plan to calculate a quality flag for all moments based on the energy and angle of the center of the peak of the distribution, and the thermal width, but this only works subject to the assumption that we can measure enough of the core of the distribution to determine those parameters accurately.

The electrostatic potential of the spacecraft affects all charged particle measurements, including those from SWIA. In most environments, the bus should float at a negative or a small positive potential, such that the charging will not result in a loss of a significant portion of the distribution. Therefore, in many regimes, LPW measurements of the spacecraft potential should allow correction of the SWIA measurements. However, in regions where the spacecraft charges to a sufficiently large positive potential to exclude a portion of the ion distribution, one cannot recover the lost information, no matter how good the knowledge of the spacecraft potential. Worse yet, exposed insulators and biased surfaces (for instance, on the solar panels and high gain antenna) can lead to differential charging that will distort the trajectories of low energy ions.

Background rates from penetrating particles also affect virtually all charged particle measurements. Mars has a rather benign energetic particle environment, greatly reducing concerns about such effects; however, during solar energetic particle events high background count rates can make interpretation of data from MCP-based instruments like SWIA without either anti-coincidence (e.g. Wind EESA-H) or coincidence (e.g. STATIC) systems challenging.

A more operational constraint results from compromises regarding the automation that controls the attenuator and telemetry mode. As described in Sect. 4.1.3, we anticipate imposing long timeouts between both attenuator actuations and telemetry mode changes, in order to prevent oscillations in the instrument state due to, for instance, plasma waves or crossings of a moving boundary. However, this also means that, at some times, the instrument may stay in the wrong state to make optimum measurements for some number of minutes. We plan to tune mode and attenuator threshold parameters in order to minimize the impact of this effect.

As mentioned in Sect. 4.1.1, the onboard energy spectra represent a simple sum over all angles in the P1 product, with no regard for the variation in geometric factor over the field of view. Therefore, one should only use these spectra in a quantitative fashion with a great degree of care; preferably, one should primarily use them as a diagnostic. With the attenuator closed, this holds doubly true, since without additional information about the distribution of the P1 counts in phi angle, one cannot even determine the overall normalization for the spectra. We can recover this information from 3d distributions, but these have lower time cadence, requiring interpolation in time to perform any corrections. SWIA ground software assumes that the majority of the counts in the spectra lie in the attenuated portion of the field of view, as expected given that the attenuator should not generally close except in the solar wind.

A final issue impacts a small fraction of the spectra and moments. For these two data sets, a single packet contains multiple data products. Each packet contains information in the header describing the telemetry mode and attenuator state. However, if either or both of these values changes in the middle of the packet, up to 15 samples can have ambiguous mode and attenuator state. The former parameter affects the de-commutation of the moments, and the latter affects the normalization of both spectra and moments. By searching for sudden jumps in the de-commutated data for the few packets thus affected, we can correct for this ambiguity in some cases; however, some small percentage of moment and spectra packets may prove unusable.

5 Conclusions

The SWIA instrument makes a key measurement for the MAVEN mission, providing the energy input from the solar wind that in part drives atmospheric escape from the Martian system. In addition to its important role for MAVEN science, SWIA can operate as a beacon for heliospheric space weather research, providing a new data point for comparison to other solar wind measurements, including L1 and 1-AU assets such as Wind, ACE, and STEREO. For MAVEN, SWIA provides measurements of solar wind ions both in the undisturbed upstream solar wind and in the post-shock magnetosheath. SWIA's design provides high energy, angular, and temporal resolution, and a very high dynamic range, allowing it to make high-quality measurements over the full range of conditions MAVEN could encounter, ranging from the highest fluxes from extreme events to the lowest fluxes from slow stagnated flows deep in the magnetosheath. SWIA also plays a role as part of a comprehensive suite of plasma instrumentation that will fully characterize the state of the Martian ionosphere and magnetosphere, the non-thermal ion escape channels that operate there, and how they depend on time, location, and external drivers. SWIA does not operate as a stand-alone instrument, but provides a critical piece of the overall puzzle for MAVEN.

Acknowledgements This paper and the SWIA instrument are dedicated to the memory of my advisor and mentor Bob Lin, without whose vision and drive the MAVEN mission would not have existed in its present form, and without whom I would not have been given the chance to participate in this mission.

References

- M.H. Acuña, J.E.P. Connerney, N.F. Ness et al., Global distribution of crustal magnetization found by the Mars Global Surveyor MAG/ER experiment. *Science* **284**, 790 (1999)
- L.A. Andersson, R.E. Ergun, G.T. Delory, A. Erickson, The Langmuir probe instrument on MAVEN. *Space Sci. Rev.* (2014, this issue)
- D.A. Brain, J.S. Halekas, R.J. Lillis, D.L. Mitchell, R.P. Lin, D.H. Crider, Variability of the altitude of the Martian sheath. *Geophys. Res. Lett.* **32**, L18203 (2005). doi:[10.1029/2005GL023126](https://doi.org/10.1029/2005GL023126)
- D.A. Brain, J.S. Halekas, L.M. Peticolas, R.P. Lin, J.G. Luhmann, D.L. Mitchell, G.T. Delory, S.W. Bougher, M.H. Acuña, H. Réme, On the origin of aurorae at Mars. *Geophys. Res. Lett.* **33**, L01201 (2006). doi:[10.1029/2005GL024782](https://doi.org/10.1029/2005GL024782)
- D.A. Brain, A.H. Baker, J. Briggs, J.P. Eastwood, J.S. Halekas, T.-D. Phan, Episodic detachment of Martian crustal magnetic fields leading to bulk atmospheric plasma escape. *Geophys. Res. Lett.* **37**, L14108 (2010). doi:[10.1029/2010GL043916](https://doi.org/10.1029/2010GL043916)
- C.W. Carlson, J.P. McFadden, P. Turin, D.W. Curtis, A. Magoncelli, The electron and ion plasma experiment for FAST. *Space Sci. Rev.* **98**, 33–66 (2001)
- J. Connerney, J. Espley Sheppard, P. Lawton, R. Oliverson, The MAVEN magnetic field investigation. *Space Sci. Rev.* (2014, this issue)
- E. Dubinin, R. Lundin, O. Norberg, N. Pissarenko, Ion acceleration in the Martian tail: Phobos observations. *J. Geophys. Res.* **98**, 3991–3997 (1993)
- E. Dubinin, M. Franz, J. Woch, E. Roussos, S. Barabash, R. Lundin, J.D. Winningham, R.A. Frahm, M. Acuna, Plasma morphology at Mars: ASPERA-3 observations. *Space Sci. Rev.* **126**, 209–238 (2006)
- E. Dubinin, M. Fraenz, J. Woch, S. Barabash, R. Lundin, Long-lived auroral structures and atmospheric losses through auroral flux tubes on Mars. *Geophys. Res. Lett.* **36**, L08108 (2009). doi:[10.1029/2009GL038209](https://doi.org/10.1029/2009GL038209)
- E. Dubinin, M. Fraenz, J. Woch, T.L. Zhang, J. Wei, A. Fedorov, S. Barabash, R. Lundin, Bursty escape fluxes in plasma sheets of Mars and Venus. *Geophys. Res. Lett.* **39**, L01104 (2012). doi:[10.1029/2011GL049883](https://doi.org/10.1029/2011GL049883)
- J.P. Eastwood, D.A. Brain, J.S. Halekas, J.F. Drake, T.D. Phan, M. Øieroset, D.L. Mitchell, R.P. Lin, M. Acuña, Evidence for collisionless magnetic reconnection at Mars. *Geophys. Res. Lett.* **35**, L02106 (2008). doi:[10.1029/2007GL032289](https://doi.org/10.1029/2007GL032289)
- N.J.T. Edberg, H. Nilsson, A.O. Williams, M. Lester, S.E. Milan, S.W.H. Cowley, M. Franz, S. Barabash, Y. Futaana, Pumping out the atmosphere of Mars through solar wind pressure pulses. *Geophys. Res. Lett.* **L03107** (2010). doi:[10.1029/2010GL041814](https://doi.org/10.1029/2010GL041814)
- R.E. Ergun, L. Andersson, W.K. Peterson, D. Brain, G.T. Delory, D.L. Mitchell, R.P. Lin, A.W. Yau, Role of plasma waves in Mars' atmospheric loss. *Geophys. Res. Lett.* **L14103** (2006). doi:[10.1029/2006GL025785](https://doi.org/10.1029/2006GL025785)
- J.R. Espley, P.A. Cloutier, D.A. Brain, D.H. Crider, M.H. Acuña, Observations of low-frequency magnetic oscillations in the Martian magnetosheath, magnetic pileup region, and tail. *J. Geophys. Res.* **109**, A07213 (2004). doi:[10.1029/2003JA010193](https://doi.org/10.1029/2003JA010193)
- X. Fang, M. Liemohn, A.F. Nagy, J.G. Luhmann, Y. Ma, Escape probability of Martian atmospheric ions: controlling effects of the electromagnetic fields. *J. Geophys. Res.* **A04308** (2010). doi:[10.1029/2009JA014929](https://doi.org/10.1029/2009JA014929)
- A. Fedorov, E. Budnik, J.-A. Sauvaud et al., The structure of the Martian wake. *Icarus* **182**, 329–336 (2006)
- H. Gunell, U.V. Amerstorfer, H. Nilsson, C. Grima, M. Koepke, M. Franz, J.D. Winningham, R.A. Frahm, J. -A Sauvaud, A. Federov, N.V. Erkaev, H.K. Biernat, M. Holmström, R. Lundin, S. Barabash, Shear driven waves in the induced magnetosphere of Mars. *Plasma Phys. Control. Fusion* **50** (2008). doi:[10.1088/0741-3335/50/7/074018](https://doi.org/10.1088/0741-3335/50/7/074018)
- J.S. Halekas, J.P. Eastwood, D.A. Brain, T.D. Phan, M. Øieroset, R.P. Lin, In-situ observations of reconnection Hall magnetic fields at Mars: evidence for ion diffusion region encounters. *J. Geophys. Res.* **114**, A11204 (2009). doi:[10.1029/JA014544](https://doi.org/10.1029/JA014544)
- J.S. Halekas, D.A. Brain, J.P. Eastwood, Large amplitude compressive “sawtooth” magnetic field oscillations in the Martian magnetosphere. *J. Geophys. Res.* **116**, A07222 (2011). doi:[10.1029/2011JA016590](https://doi.org/10.1029/2011JA016590)
- B. Jakosky, R.P. Lin, J. Grebowsky, J.G. Luhmann, D.L. Mitchell, D.A. Brain, R.J. Lillis et al., The 2013 Mars Atmosphere and Volatile Evolution (MAVEN) mission to Mars. *Space Sci. Rev.* (2014, this issue)
- E. Kallio, J.G. Luhmann, S. Barabash, Charge exchange near Mars: solar wind absorption and energetic neutral atom production. *J. Geophys. Res.* **102**, 22183–22197 (1997)
- H. Lammer, S.J. Bauer, Nonthermal atmospheric escape from Mars and Titan. *J. Geophys. Res.* **96**, 1819–1825 (1991)
- D.E. Larson, R.J. Lillis et al., The MAVEN Solar Energetic Particle instrument. *Space Sci. Rev.* (2014, this issue)

- F. Leblanc, R.E. Johnson, Sputtering of the Martian atmosphere by solar wind pick-up ions. *Planet. Space Sci.* **49**, 645–656 (2001)
- R.P. Lin, K.A. Anderson, S. Ashford, C. Carlson, D. Curtis, R. Ergun, D. Larson, J. McFadden, M. McCarthy, G.K. Parks, H. Reme, J.M. Bosqued, J. Coutelier, F. Cotin, C. D’Uston, K.-P. Wenzel, T.R. Sanderson, J. Henrion, J.C. Ronnet, G. Paschmann, A three-dimensional plasma and energetic particle investigation for the Wind spacecraft. *Space Sci. Rev.* **71**, 125–153 (1995)
- R. Lundin, A. Zakharov, R. Pellinen, S.W. Barabash, H. Borg, E.M. Dubinin, B. Hultqvist, H. Koskinen, I. Liede, N. Pissarenko, ASPERA/Phobos measurements of the ion outflow from the Martian ionosphere. *Geophys. Res. Lett.* **17**, 873–876 (1990)
- R. Lundin, D. Winningham, S. Barabash et al., Plasma acceleration above Martian magnetic anomalies. *Science* **311**, 980–983 (2006)
- R. Lundin, S. Barabash, M. Holmstrom, H. Nilsson, M. Yamauchi, M. Fraenz, E.M. Dubinin, A comet-like escape of ionospheric plasma from Mars. *Geophys. Res. Lett.* **35** (2008). doi:[10.1029/2008GL034811](https://doi.org/10.1029/2008GL034811)
- J.G. Luhmann, J.U. Kozyra, Dayside pickup oxygen ion precipitation at Venus and Mars—spatial distributions, energy deposition and consequences. *J. Geophys. Res.* **96**, 5457–5467 (1991)
- D.L. Mitchell, C. Mazelle, J.A. Sauvaud, D. Toubanc, Thocaven, Rouzard, A. Federov, E.R. Taylor, M. Robinson, P. Turin, D.W. Curtis, The MAVEN Solar Wind Electron Analyzer (SWEA). *Space. Sci. Rev.* (2014, this issue)
- J.P. McFadden, C.W. Carlson, D. Larson, M. Ludlam, R. Abiad, B. Elliott, P. Turin, M. Marckwordt, V. Angelopoulos, The THEMIS ESA plasma instrument and in-flight calibration. *Space Sci. Rev.* **141**, 277–302 (2008)
- J.P. McFadden et al., *Space Sci. Rev.* (2014, this issue)
- A.F. Nagy, D. Winterhalter, K. Sauer, T.E. Cravens, S. Brecht, C. Mazelle, D. Crider, E. Kallio, A. Zakharov, E. Dubinin, M. Verigin, G. Kotova, W.I. Axford, C. Bertucci, J.G. Trotignon, The plasma environment of Mars. *Space Sci. Rev.* **111**, 33 (2004)
- T. Penz, N.V. Erkaev, H.K. Biernat, H. Lammer, U.V. Amerstorfer, H. Gunell, E. Kallio, S. Barabash, S. Orsini, A. Milillo, W. Baumjohann, Ion loss on Mars caused by the Kelvin-Helmholtz instability. *Planet. Space Sci.* **52**, 1157–1167 (2004)
- H. Rème, J.M. Bosqued, J.A. Sauvaud et al., The cluster ion spectrometry (CIS) experiment. *Space Sci. Rev.* **79**, 303–350 (1997)
- M.H.G. Zhang, J.G. Luhmann, A.F. Nagy, J.R. Spreiter, S.S. Stahara, Oxygen ionization rates at Mars and Venus: relative contributions of impact ionization and charge exchange. *J. Geophys. Res.* **98**, 3311–3318 (1993)